Optical Materials 108 (2020) 110194

Contents lists available at ScienceDirect

Optical Materials

journal homepage: http://www.elsevier.com/locate/optmat

Improving the photostability of printed organic photovoltaics through luminescent solar concentrators

Yilin Li [a,*], Yujian Sun [b], Yongcao Zhang [c], Wen-Ji Dong [d]

[a] Department of Chemical and Biomolecular Engineering, Rice University, Houston, TX, 77005, United States
[b] School of Environmental and Forest Sciences, University of Washington, Seattle, WA, 98195, United States
[c] Department of Mechanical Engineering, University of Houston, Houston, TX, 77004, United States
[d] School of Chemical Engineering and Bioengineering, Washington State University, Pullman, WA, 99164, United States

ARTICLE INFO

Keywords:
Photostability
Large-area
Printed
Organic photovoltaics
Luminescent solar concentrators
Power conversion efficiency

ABSTRACT

In this study, we propose to improve the photostability of large-area (up to 19.35 cm^2) printed organic photovoltaics (OPVs) through luminescent solar concentrators (LSCs), which convert high-energy short-wavelength (λ < 600 nm) photons to low-energy long-wavelength (λ > 600 nm) photons. We investigate the impacts of the luminophore concentration and waveguide surface roughness on the power conversion efficiency (PCE) of the OPV-LSCs with sizes from 1 inch (2.54 cm) to 12 inches (30.48 cm), corresponding to front surface areas from 6.4516 cm^2 to 929.0304 cm^2. For the 6-inch (232.26-cm^2) OPV-LSCs, the results show that a high waveguide surface roughness (R_q = 63 nm) leads to devices with a high device PCE (η_{LSC} = 0.93%) and wide external quantum efficiency (EQE) from 400 nm to 800 nm. Detailed edge emission analysis on the luminescent waveguides indicates an edge emission with a large fraction (>95%) of long-wavelength photons comprised of a large fraction (>25%) of near-infrared (NIR) (λ > 700 nm) light. This leads to the photostability (defined as the hours when the PCE drops by 10%) of the OPV-LSCs significantly improved to 320 h under continuous 1 sun illumination (the photostability of the OPVs is only 25 h). The approach of OPV-LSCs paves the way to practically improve the photostability of large-area printed OPVs.

1. Introduction

The research efforts toward the technology development for eco-friendly energy have been accelerated in the past decade owing to concerns of global warming and environmental issues [1–3]. Among various eco-friendly technologies, photovoltaic (PV) technologies, that enable the direct generation of electricity from light, have demonstrated significant potential for satisfying the growing demand for clean and renewable energy [4–6]. Organic PVs (OPVs), which utilize light-absorbing organic materials, have received a lot of attention because they offer the attractive prospect of low-temperature, solution-processed fabrication such as roll-to-roll and inkjet printing, which have the potential to dramatically lower the cost of solar energy production [7–9]. While numerous advancements have been made and OPVs with power conversion efficiency (PCE) comparable to conventional silicon-based PVs have been achieved in recent years, challenges remain in developing devices with high photostability, especially for large-area devices [10–12]. One of the primary reasons for the photodegradation of the OPVs is the absorption of short-wavelength (λ < 600 nm) photons. Short-wavelength photons are high-energy photons that release a large amount of heat during the photoelectric conversion, which warms up the devices and changes the physical and chemical properties of organic materials, and eventually affects the performance of the OPVs.

An effective approach to circumventing this issue is to convert short-wavelength photons to long-wavelength (λ > 600 nm) photons before the photoelectric conversion [13–15], which has been successfully applied to improve the operational stability of organic and organic-inorganic hybrid PVs [16,17]. The long-wavelength photons are low-energy photons that release much less heat during the photoelectric conversion than the short-wavelength photons. A good platform for the wavelength conversion is the luminescent solar concentrator (LSC) as shown in Fig. 1a. A typical LSC consists of a luminophore-doped waveguide with PV cells attached to the edge of the waveguide [18–20]. The luminophores absorb short-wavelength photons and emit long-wavelength photons inside the waveguide, which follow total

* Corresponding author.
E-mail address: yilinli@rice.edu (Y. Li).

https://doi.org/10.1016/j.optmat.2020.110194
Received 10 May 2020; Received in revised form 14 June 2020; Accepted 4 July 2020

internal reflection (TIR), reach the edge of the waveguide, and are absorbed by the edge-attached PV cells. This design allows LSCs to show the capability to transform exterior building parts such as windows, facades, and atriums into energy-harvesting devices, which enables the possibility to harvest solar energy almost everywhere within our community [21–23]. Moreover, their capabilities of harvesting direct and diffused light and being designed with different colors and shapes have enabled them to be utilized in various outdoor and indoor environments [24–26].

In this study, we fabricated the large-area (up to 19.3548 cm^2) printed OPVs and integrated them with the LSCs. In this system, the OPVs only absorb low-energy long-wavelength photons that are delivered by the luminescent waveguide, as shown in Fig. 1b, and therefore the photostability of the OPVs is improved. Two different luminophore concentrations were used in the waveguide and surface scattering treatment (SST) was applied to the waveguide to adjust the percentage of long-wavelength photons in the edge emission of the waveguide. Highly photostable OPV-LSCs were achieved with only a 10% drop in the original PCE after continuous 1 sun illumination for 320 h.

2. Experimental

2.1. Materials and instrumentations

All chemicals were used as received without further purification. The ITO-coated glass substrates, PEDOT:PSS (Clevios P VP Al 4083, Heraeus), $PC_{70}BM$, 1,8-diiodooctane (DIO), bathocuproine (BCP), monomer methyl methacrylate (MMA), azobisisobutyronitrile (AIBN), and ethylene vinyl acetate (EVA) were purchased from Sigma-Aldrich. The luminophore R305 was purchased from TCI America. The UV-curing optical adhesive was purchased from eBay.

An OAI class AAA solar simulator was used to provide simulated AM1.5G sunlight. The *J-V* characteristic curves were measured using a Keithley 2401 source meter. The power conversion efficiencies (PCEs) of the OPVs and the OPV-LSCs are defined according to the standard definition of the PCE of a PV device, which is the electric power from the device relative to the incident power on the device. The electric power was calculated from the *J-V* characteristic curve of the device measured under AM1.5G simulated sunlight with a power density of 1000 W m^{-2}. The external quantum efficiency (EQE) spectra of the OPVs and the OPV-LSCs were performed on an Enlitech QE-R3011 system. The absorption spectrum of R305 was measured using a Varian Cary 5000 UV–Vis–NIR spectrometer. The emission spectrum of R305 was recorded on an ISS PC1 photon-counting spectrofluorometer. The edge emission spectrum of the waveguide was measured using an integrating sphere connected to a Hamamatsu C9920-12 EQE measurement system. The photostability of the OPVs and the OPV-LSCs were tested according to the ISOS (international summit on OPV stability) protocol [27].

2.2. Fabrication of the OPVs

The fabrication of the large-area printed OPVs is according to literature [28–30]. The chemical structure of the small-molecule donor, LGC-D023 [31], used in the OPVs, is shown in Fig. 2a. The energy diagram of the components in the OPVs is depicted in Fig. 2b. The ITO-coated large-area (4 × 4 in^2, 10.16 × 10.16 cm^2) glass substrates were exposed to UV/ozone for 15 min. PEDOT:PSS was spin-coated at 5000 rpm for 40 s and then thermally annealed at 150 °C for 10 min to form the hole-transport layer. The active layer solution was prepared by mixing LGC-D023 and $PC_{70}BM$ (1:2, w/w) in chlorobenzene with DIO (3%, v/v%). Then, the active layer solution was slot-die coated on the top of the hole-transport layer under the ambient condition at a coating speed of 12 mm s^{-1}, as illustrated in Fig. 2c [32]. An additional N_2 blowing system was introduced to produce uniform and defect-free optimized organic films [33]. Finally, BCP (3 nm) and Ag (80 nm) layers were deposited on the top of the active layer by thermal evaporation. The module was cut and reconnected in parallel to fit the edge size of waveguide (0.25 × 1–12 in^2, 0.635 × 2.54–30.48 cm^2). The OPVs were encapsulated using EVA according to the literature [34,35].

2.3. Fabrication of the LSCs

The LSCs used in this study are red-emission LSCs as depicted in Fig. 2d. The fabrication of the LSCs was according to the literature [36]. As shown in Fig. 2e, A solution containing R305 (7.5 or 760 ppm, corresponding to the optical density (OD) of the luminescent waveguides being 1.0 or 4.0) and AIBN (0.1%, w/w%) in MMA was pre-polymerized at 85 °C for approximately 10 min. The glycerol-like viscous syrup was poured into a glass mold and further polymerized at 45 °C for 48 h, following by full polymerization at 100 °C for 2 h. The resulting raw waveguide was processed by mechanical power tools to a square-shaped waveguide. The thickness was 0.25 inch, and the size was from 1 inch (2.54 cm) to 12 inches (30.48 cm), corresponding to a front surface area from 6.4516 cm^2 to 929.0304 cm^2. The OPVs were then attached to the edge of the waveguide using UV-curing optical adhesive. They were connected in parallel to maximize device performance [37]. The geometric factor (*G*) of the devices is from 1 to 12, which is numerically equal to the device size (*L*). In this report, we present *L* instead of *G* because *L* directly reflects how large the device is.

3. Results and discussion

3.1. PV performance of the OPVs

Before attaching the OPVs to the waveguides, we first look at the PV performance of the OPVs. In our study, the largest area for the printed OPVs is 19.3548 cm^2, which matches the edge area of the 12-inch (929.0304-cm^2) luminescent waveguide. As shown in Fig. 3a, the power conversion efficiency of the OPVs (PCE) (η_{cell}) is 4.44%. The corresponding short-circuit current density ($J_{sc,cell}$), open-circuit voltage ($V_{oc,cell}$), and fill factor (FF_{cell}) are 90 A m^{-2}, 0.80 V, and 0.62, respectively, which are consistent with the literature [30]. The external quantum efficiency of OPV (EQE_{cell}) ranges from 300 nm to 800 nm, and the values are below 0.50, as depicted in Fig. 3b. The low EQE_{cell} values

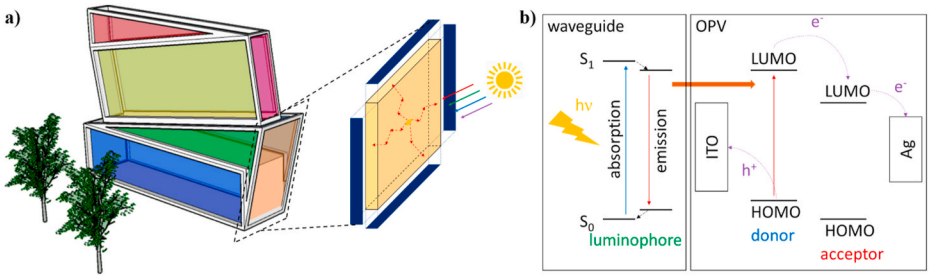

Fig. 1. a) Schematic representation of the application and architecture of the LSCs. **b)** Energy diagram showing the delivery of low-energy long-wavelength photons from the luminescent waveguide to the OPVs.

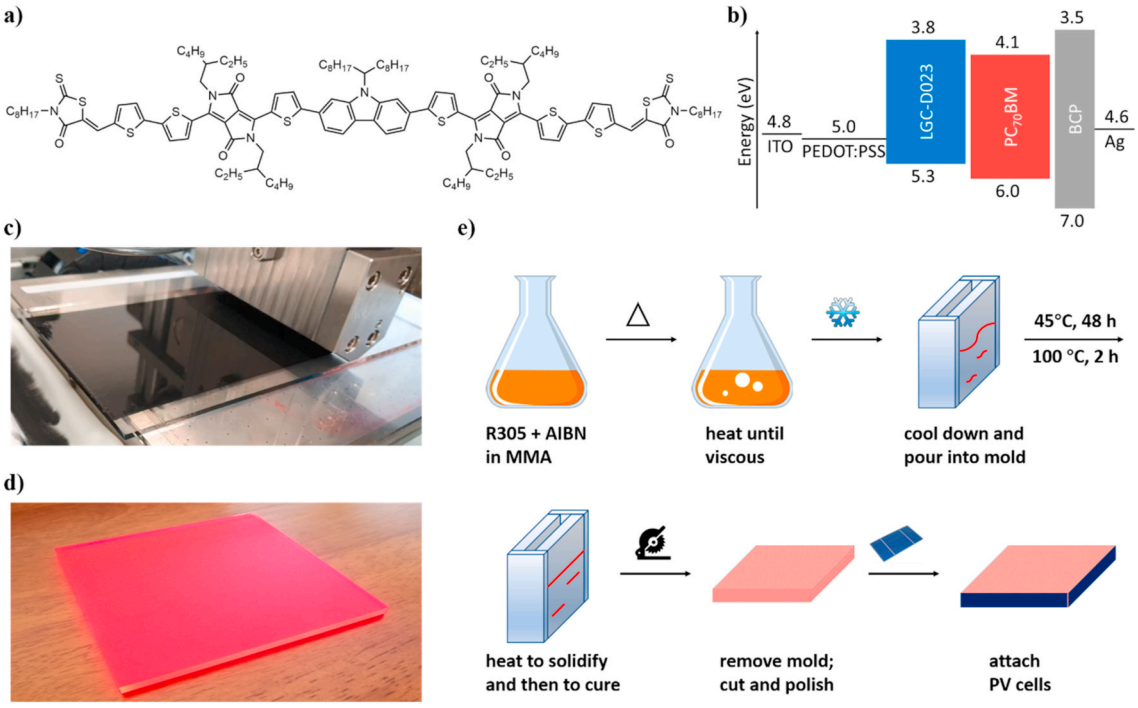

Fig. 2. **a)** Chemical structure of LGC-D023. **b)** Energy level diagram of the components in the OPVs. Pictures showing **c)** the slot-die coating process of the OPVs and **d)** the red-emission LSCs. **e)** The fabrication process of the LSCs. (For interpretation of the references to color in this figure legend, the reader is referred to the Web version of this article.)

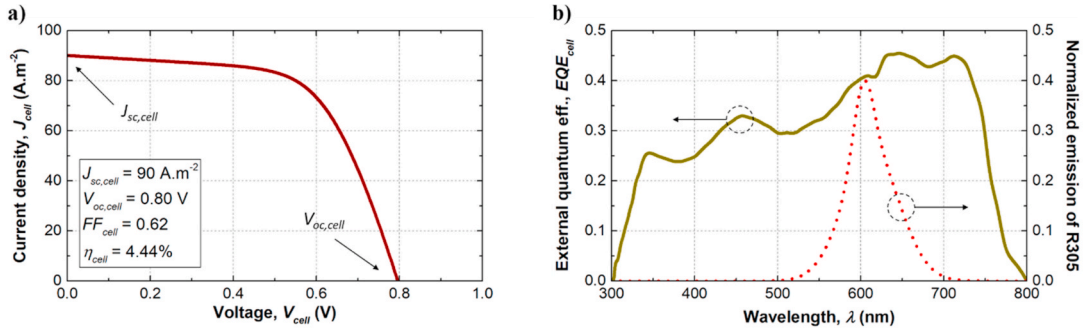

Fig. 3. **a)** *J-V* characteristic curve of the OPVs. **b)** EQE_{cell} superimposed with the normalized emission spectrum of R305.

are possibly due to the large device area, which is typically associated with high internal resistance caused by a large amount of electron-hole recombination [38,39]. The EQE_{cell} shows a relatively weak response (<0.4) to the incidence below 600 nm but a relatively strong response (>0.4) beyond 600 nm, which suggests that the long-wavelength photon is more favorable to the OPVs than short-wavelength photons. The emission spectrum of R305 ranges from 500 nm to 700 nm and centers at 605 nm, which is close to the strong response region of EQE_{cell}, which indicates that the R305-based waveguides are suitable for the OPVs.

3.2. PV performance of the OPV-LSCs

After having the PV performance of the OPVs, we then attached the OPVs to the luminescent waveguides and measured the power conversion efficiency (PCE) of the OPV-LSCs (η_{LSC}) with sizes (L) from 1 inch (2.54 cm) to 12 inches (30.48 cm), corresponding to front surface areas from 6.4516 cm^2 to 929.0304 cm^2. The OPV-LSCs were investigated using two luminophore concentrations (C): a low concentration of 7.5 ppm and a high concentration of 60 ppm. Surface scattering treatment (SST) was applied to the luminescent waveguides to investigate the scattering effect on the PV performance of the OPV-LSCs. The detailed procedures for the SST are described in the literature [40]. The root-mean-squared surface roughness (R_q) of the front surface of the luminescent waveguides changes is 15 and 63 nm before and after the SST.

The relationships between the η_{LSC} and the L before (R_q = 15 nm) and after (R_q = 63 nm) the SST are depicted in Fig. 4a and b, respectively. The overall results show that, the η_{LSC} decreases with the increase of the L regardless of the C and the SST, suggestive of the increase of the photon energy loss. Before the SST, increasing the C significantly improves the η_{LSC}. For example, for the 6-inch (232.2576-cm^2) devices, the η_{LSC} is increased from 0.75% to 0.89% (approximately +19%) when the C is increased from 7.5 ppm to 60 ppm, which is due to the increase of the number of photons absorbed and converted by the luminophores. After the SST, increasing the C does not improve the η_{LSC} much, and the improvement becomes less and less with the increase of the L. For example, the 6-inch devices exhibit a η_{LSC} of 0.93% despite the C being increased from 7.5 ppm to 60 ppm. This is because the scattering effect disturbs the total internal reflection (TIR)-based transport of the luminophore-emitted photons within the waveguide. The improvement

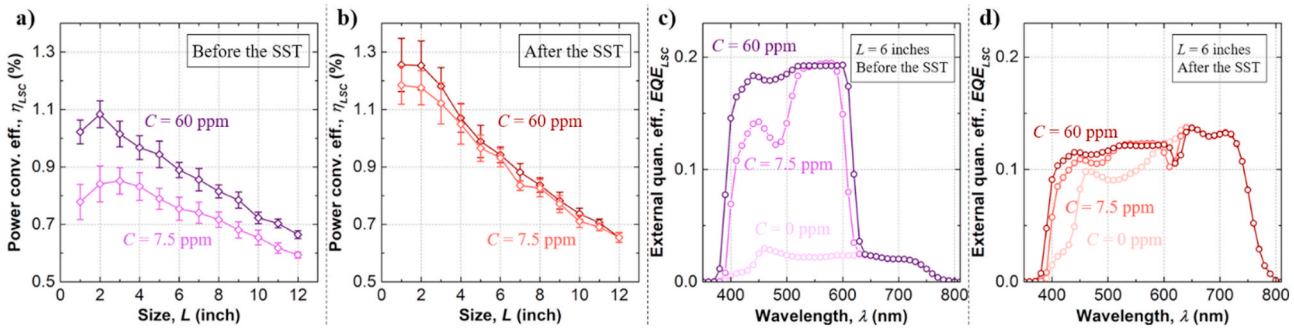

Fig. 4. The relationship between the η_{LSC} and the L for the devices with C of 7.5 and 60 ppm **a)** before and **b)** after the SST. The EQE_{LSC} for devices with C of 0, 7.5, and 60 ppm **c)** before and **d)** after the SST.

in the η_{LSC} after the SST indicates the beneficial impact of the scattering effect, and the impact is more evident in small-area (L < 4 inches or 10.16 cm) devices. This is because the SST enhances the device performance through the scattering mechanism, while the small-area devices exhibit less scattering loss and less luminophore self-absorption loss than the large-area devices [40,41].

To further understand the PV performance of the OPV-LSCs, we measured the external quantum efficiency (EQE) of the devices (EQE_{LSC}). The results for the 6-inch devices before and after the SST are presented in Fig. 4c and d, respectively. The spectral range of the EQE_{LSC} is up to 800 nm, beyond which the OPVs do not exhibit any photon absorption (Fig. 3b). Before the SST, increasing the C significantly improves the EQE_{LSC}, especially below 550 nm. The relatively high EQE_{LSC} from 350 nm to 620 nm is primarily due to the photon conversion of the luminophores. The relatively low EQE_{LSC} from 620 nm to 800 nm is primarily due to the scattering effect, which is evidenced in the overlap with the EQE_{LSC} of the blank (C = 0 ppm) device. The EQE_{LSC} between 550 nm and 600 nm is independent of C, which is possibly due to the scattering effect that disturbs the photon absorption. After the SST, the EQE_{LSC} becomes broader, and the impact of the C becomes minimal. A majority of the EQE_{LSC} is from the scattering effect as it overlaps a lot with the EQE_{LSC} of the blank device. Though the photon conversion of the luminophores is affected by the scattering effect, it contributes to the EQE_{LSC} below 620 nm, which balances the region of the photon conversion (λ = 350–620 nm) with the region of the scattering effect (λ = 620–800 nm). This balance suggests the beneficial impact of the SST on the PV performance of the OPV-LSCs.

3.3. Edge emission of the luminescent waveguides

The difference in the EQE_{LSC} for 6-inch (232.26-cm^2) OPV-LSCs encouraged us to investigate the edge emission of the luminescent (C = 7.5 and 60 ppm) waveguides before (R_q = 15 nm) and after (R_q = 63 nm) the SST. To compare the edge emission of the luminescent waveguides under different conditions in a fair way, the measured edge emission spectrum was normalized over the spectral area from 600 nm to 800 nm and then multiplied with the short-circuit current density of the OPV-LSCs ($J_{sc,LSC}$). The edge emission of the blank (C = 0 ppm) waveguides before and after the SST was also measured to understand the role of the SST in the edge emission of the luminescent waveguides.

As shown in Fig. 5a, before the SST, the edge emission of the blank waveguides is very weak, and the spectrum ranges from 400 nm to 800 nm. For the luminescent waveguides as depicted in Fig. 5b, the short-wavelength (λ < 600 nm) photons are down-shifted to long-wavelength (λ > 600 nm) photons, and the spectrum primarily ranges from 600 nm to 800 nm. The red-shifted edge emission with higher intensity for the luminescent waveguides with higher luminophore concentration indicates the increased self-absorption of the luminophores. The spectral tail between 700 nm and 800 nm suggests a low degree of scattering effect. The edge emission changes significantly for the luminescent waveguides after the SST. As shown in Fig. 5c, the blank waveguides exhibit significantly enhanced emission intensity from 400 nm to 800 nm. For the luminescent waveguides as depicted in Fig. 5d, the edge emission shows distinctive scattering peaks (700–800 nm) besides the emission peak of the luminophores. The broad edge emission comprised of a large fraction of scattering peaks leads to similar EQE_{LSC} for the devices with C of 7.5 and 60 ppm after the SST.

The spectral properties of the edge emission for the blank and the luminescent waveguides before and after the SST are listed in Table 1. Before the SST, the edge emission power density of the blank waveguides is 164 W m^{-2}, comprised of a large fraction (55%) of short-wavelength photons and nearly balanced fractions of long-wavelength visible (25%) and near-infrared (NIR) (20%) photons. The edge emission power densities of the luminescent waveguides with C of 7.5 and 60 ppm are 452 and 529 W m^{-2}, respectively, comprised of a large fraction (>90%) of long-wavelength visible photons. After the SST, the edge emission power density of the blank waveguides is significantly increased to 938 W m^{-2}, with the fraction of the short-wavelength and long-wavelength photons minimally changed. The edge emission power densities of the luminescent waveguides with C of 7.5 and 60 ppm are

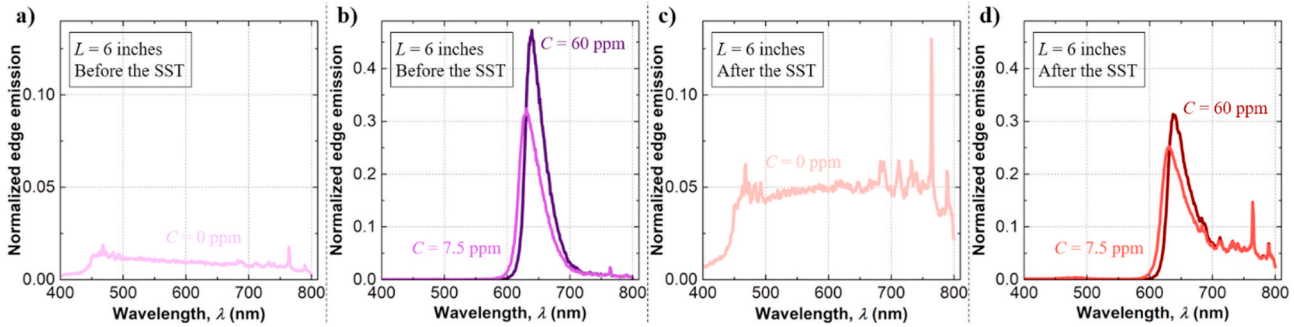

Fig. 5. Normalized edge emission spectra of the blank and luminescent waveguides before and after the SST.

Table 1
Spectral properties of the edge emission spectra of the blank and luminescent waveguides before and after the SST.

	C	Edge emission power density (400–800 nm)	Percentage of short-wavelength photons	Percentage of long-wavelength photons		
			Visible (400–600 nm)	Visible (600–700 nm)	NIR (700–800 nm)	NIR/visible ratio
Before the SST	0 ppm	164 W m^{-2}	55%	25%	20%	0.8
	7.5 ppm	452 W m^{-2}	1%	92%	7%	0.076
	60 ppm	529 W m^{-2}	0%	94%	6%	0.064
After the SST	0 ppm	938 W m^{-2}	43%	29%	28%	0.97
	7.5 ppm	856 W m^{-2}	3%	68%	29%	0.43
	60 ppm	853 W m^{-2}	0%	71%	29%	0.41

856 and 853 W m^{-2}. The fraction of the NIR photons is significantly increased to 29%, and the visible/NIR ratio is also increased to over 0.4. The large fraction (>95%) of the long-wavelength photons comprised of a large fraction (>25%) of NIR photons for the luminescent waveguides after the SST would be beneficial to the photostability of the OPVs when attached to the luminescent waveguides.

3.4. Photostability of the OPVs and the OPV-LSCs

Our final task is to examine the photostability of the OPVs and the OPV-LSCs. As shown in Fig. 6a, the OPVs exhibit a fast decay in the η_{cell} with the increase of the illumination time (t) under continuous 1 sun (1000 W m^{-2}) illumination. The photostability (defined as the hours when the PCE drops by 10%) of the OPVs is 25 h, which is consistent with a previous report [30] and due to the use of DIO during the device fabrication [42]. The η_{cell} drops to below 80% of the original value after 120 h and finally reaches 70% of the original value at 320 h.

The initial η_{LSC} for the OPV-LSCs in the photostability test is given in Fig. 6b. Before the SST (R_q = 15 nm), the initial η_{LSC} are 0.17%, 0.75%, and 0.89% for C of 0, 7.5, and 60 ppm, respectively. The low η_{LSC} for C of 0 ppm is due to the low edge emission power density of 164 W m^{-2} (Table 1). After the SST (R_q = 63 nm), the η_{LSC} for C of 0 ppm is increased to 0.88% as the edge emission power density is significantly increased to 938 W m^{-2} (Table 1) due to the scattering effect. The η_{LSC} for C of 7.5 and 60 ppm are also increased to 0.93% and 0.94%, respectively.

Before the SST, the photostability of the OPV-LSCs for C of 0, 7.5, and 60 ppm are 40, 50, and 60 h, respectively, as shown in Fig. 6c. The improved photostability of devices with C of 0 ppm (40 h) compared with the photostability of the OPVs (25 h) is due to the low edge emission power density (Fig. 6b). However, it is still lower than the photostability of the devices with C of 7.5 (50 h) and 60 ppm (60 h), because of a large fraction (55%) of short-wavelength (λ < 600 nm) photons in the edge emission (Table 1). After the SST, the photostability of the devices with C of 0 ppm drops to 33 h, which is close to the photostability of the OPVs (25 h) due to a high edge emission power density (938 W m^{-2}) with a large fraction (43%) of the short-wavelength photons (Table 1). The photostability of the devices with C of 7.5 and 60 ppm are significantly improved to 213 and 320 h, respectively, despite higher edge emission power densities (>850 W m^{-2}) than those before the SST (<550 W m^{-2}) (Table 1). The results suggest that a large fraction (>95%) of long-wavelength (λ > 600 nm) photons with a large fraction (>25%) of NIR (700–800 nm) photons is a more decisive factor on the photostability of the OPV-LSCs compared with the edge emission power density. Therefore, the highest photostability of the devices with C of 7.5 ppm after the SST is primarily due to a large fraction (97%) of long-wavelength photons with a high NIR/visible ratio (0.43) (Table 1).

4. Conclusions

In summary, we applied large-area (up to 19.3548 cm^2) printed organic photovoltaics (OPVs) to luminescent solar concentrators (LSCs) and addressed the poor photostability of the OPVs through the wavelength conversion of the luminophores, which converted high-energy short-wavelength (λ < 600 nm) photons to low-energy long-wavelength (λ > 600 nm) photons. The PV performance of the OPV-LSCs was investigated for the devices with luminophore concentrations of 7.5 and 60 ppm before and after the surface scattering treatment (SST). The results for the EQE measurement on the 6-inch (232.2576-cm^2) devices after the SST showed a significantly enhanced long-wavelength response region (600–800 nm). The analysis on edge emission of the luminescent waveguide indicated a large fraction of NIR (700–800 nm) photons of up to 29%. The photostability of the OPVs was significantly improved through the integration with the LSCs. The OPV-LSCs with a C of 7.5 ppm after the SST sustained 90% of the original PCE after 320 h of continuous 1 sun illumination. This was significantly longer than the OPVs, which exhibited a 90% drop in PCE after 25 h of continuous 1 sun illumination.

Declaration of competing interest

The authors declare that they have no known competing financial interests or personal relationships that could have appeared to influence

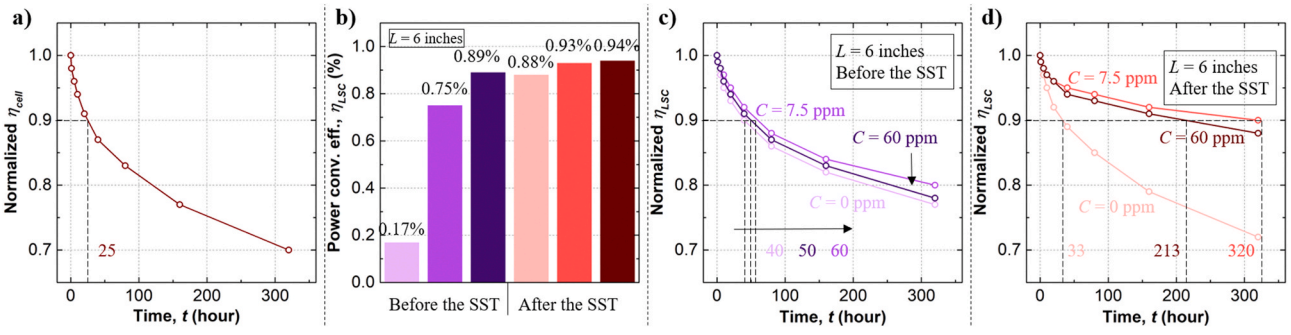

Fig. 6. Photostability of the OPVs, and the initial η_{LSC} and the photostability of the OPV-LSCs before and after the SST.

the work reported in this paper.

CRediT authorship contribution statement

Yilin Li: Conceptualization, Writing - review & editing, Supervision. **Yujian Sun:** Investigation, Writing - original draft, Visualization. **Yongcao Zhang:** Software, Formal analysis, Data curation. **Wen-Ji Dong:** Resources, Data curation, Writing - review & editing.

Acknowledgments

This work is a part of the project: Energy-harvesting windows and panels. The authors would like to thank Solera City Energy for research support.

References

[1] I. Dincer, Renewable energy and sustainable development: a crucial review, Renew. Sustain. Energy Rev. 4 (2000) 157–175, https://doi.org/10.1016/S1364-0321(99)00011-8.
[2] N.L. Panwar, S.C. Kaushik, S. Kothari, Role of renewable energy sources in environmental protection: a review, Renew. Sustain. Energy Rev. 15 (2011) 1513–1524, https://doi.org/10.1016/j.rser.2010.11.037.
[3] P.A. Owusu, S. Asumadu-Sarkodie, A review of renewable energy sources, sustainability issues and climate change mitigation, Cogent Eng 3 (2016) 1167990, https://doi.org/10.1080/23311916.2016.1167990.
[4] B. Parida, S. Iniyan, R. Goic, A review of solar photovoltaic technologies, Renew. Sustain. Energy Rev. 15 (2011) 1625–1636, https://doi.org/10.1016/j.rser.2010.11.032.
[5] L.E. Chaar, L.A. lamont, N.E. Zein, Review of photovoltaic technologies, Renew. Sustain. Energy Rev. 15 (2011) 2165–2175, https://doi.org/10.1016/j.rser.2011.01.004.
[6] R. Luthander, J. Widén, D. Nilsson, J. Palm, Photovoltaic self-consumption in buildings: a review, Appl. Energy 142 (2015) 80–94, https://doi.org/10.1016/j.apenergy.2014.12.028.
[7] N. Kaur, M. Singh, D. Pathak, T. Wagner, J.M. Nunzid, Organic materials for photovoltaic applications: review and mechanism, Synth. Met. 190 (2014) 20–26, https://doi.org/10.1016/j.synthmet.2014.01.022.
[8] J. Yu, Y. Zheng, J. Huang, Towards high performance organic photovoltaic cells: a review of recent development in organic photovoltaics, Polymers 6 (2014) 2473–2509, https://doi.org/10.3390/polym6092473.
[9] S. Holliday, Y. Li, C.K. Luscombe, Recent advances in high performance donor-acceptor polymers for organic photovoltaics, Prog. Polym. Sci. 70 (2017) 34–51, https://doi.org/10.1016/j.progpolymsci.2017.03.003.
[10] S. Lizin, S.V. Passel, E.D. Schepper, W. Maes, L. Lutsen, J. Manca, D. Vanderzande, Life cycle analyses of organic photovoltaics: a review, Energy Environ. Sci. 6 (2013) 3136–3149, https://doi.org/10.1039/C3EE42653J.
[11] S.A. Gevorgyan, M.V. Madsen, B. Roth, M. Corazza, M. Hösel, R.R. Søndergaard, M. Jørgensen, F.C. Krebs, Lifetime of organic photovoltaics: status and predictions, Adv. Energy Mater. 6 (2016) 1501208, https://doi.org/10.1002/aenm.201501208.
[12] W.R. Mateker, M.D. McGehee, Progress in understanding degradation mechanisms and improving stability in organic photovoltaics, Adv. Mater. 29 (2017) 1603940, https://doi.org/10.1002/adma.201603940.
[13] Y. Li, Z. Li, Y. Wang, A. Compaan, T. Ren, W.-J. Dong, Increasing the power output of a CdTe solar cell via luminescent down shifting molecules with intramolecular charge transfer and aggregation-induced emission characteristics, Energy Environ. Sci. 6 (2013) 2907–2911, https://doi.org/10.1039/C3EE42001A.
[14] Y. Li, Z. Li, T. Ablekim, T. Ren, W.-J. Dong, Rational design of tetraphenylethylene-based luminescent down-shifting molecules: photophysical studies and photovoltaic applications in a CdTe solar cell from small to large units†, Phys. Chem. Chem. Phys. 16 (2014) 26193–26202, https://doi.org/10.1039/C4CP03521F.
[15] Y. Li, J. Olsen, W.-J. Dong, Enhancing the output current of a CdTe solar cell via a CN-free hydrocarbon luminescent down-shifting fluorophore with intramolecular energy transfer and restricted internal rotation characteristics, Photochem. Photobiol. Sci. 14 (2015) 833–841, https://doi.org/10.1039/C4PP00480A.
[16] J. Kettle, N. Bristow, D.T. Gethin, Z. Tehrani, O. Moudam, B. Li, E.A. Katz, G.A.d. R. Benatto, F.C. Krebs, Printable luminescent down shifter for enhancing efficiency and stability of organic photovoltaics, Sol. Energy Mater. Sol. Cells 144 (2016) 481–487, https://doi.org/10.1016/j.solmat.2015.09.037.
[17] H.S. Anizelli, V. Stoichkov, R.V. Fernandes, J.L. Duarte, E. Laureto, J. Kettle, I. Visoly-Fisher, E.A. Katz, Application of luminescence downshifting materials for enhanced stability of $CH_3NH_3PbI_{3(1-x)}Cl_{3x}$ perovskite photovoltaic devices, Org. Electron. 49 (2017) 129–134, https://doi.org/10.1016/j.orgel.2017.06.056.
[18] M.G. Debije, P.P.C. Verbunt, Thirty years of luminescent solar concentrator research: solar energy for the built environment, Adv. Energy Mater. 2 (2012) 12–35, https://doi.org/10.1002/aenm.201100554.
[19] F. Meinardi, F. Bruni, S. Brovelli, Luminescent solar concentrators for building-integrated photovoltaics, Nat. Rev. Mater. 2 (2017) 17072, https://doi.org/10.1038/natrevmats.2017.72.
[20] Y. Li, X. Zhang, Y. Zhang, R. Dong, C.K. Luscombe, Review on the role of polymers in luminescent solar concentrators, J. Polym. Sci., Polym. Chem. Ed. 57 (2019) 201–215, https://doi.org/10.1002/pola.29192.
[21] A. Kerrouche, D.A. Hardy, D. Ross, B.S. Richards, Luminescent solar concentrators: from experimental validation of 3D ray-tracing simulations to coloured stained-glass windows for BIPV, Sol. Energy Mater. Sol. Cells 122 (2014) 99–106, https://doi.org/10.1016/j.solmat.2013.11.026.
[22] W.v. Sark, P. Moraitis, C. Aalberts, M. Drent, T. Grasso, Y. L'Ortije, M. Visschers, M. Westra, R. Plas, W. Planje, The "electric mondrian" as a luminescent solar concentrator demonstrator case study, Sol. RRL 1 (2017) 1600015, https://doi.org/10.1002/solr.201600015.
[23] A. Reinders, R. Kishore, L. Slooff, W. Eggink, Luminescent solar concentrator photovoltaic designs, Jpn. J. Appl. Phys. 57 (2018), https://doi.org/10.7567/JJAP.57.08RD10, 08RD10.
[24] F.M. Vossen, M.P.J. Aarts, M.G. Debije, Visual performance of red luminescent solar concentrating windows in an office environment, Energy Build. 113 (2016) 123–132, https://doi.org/10.1016/j.enbuild.2015.12.022.
[25] C. Corrado, S.W. Leow, M. Osborn, I. Carbone, K. Hellier, M. Short, G. Alers, S. A. Carter, Power generation study of luminescent solar concentrator greenhouse, J. Renew. Sustain. Energy 8 (2016), 043502, https://doi.org/10.1063/1.4958735.
[26] Y. Li, Y. Sun, Y. Zhang, Luminescent solar concentrators performing under different light conditions, Sol. Energy 188 (2019) 1248–1255, https://doi.org/10.1016/j.solener.2019.07.035.
[27] M.O. Reese, S.A. Gevorgyan, M. Jørgensen, E. Bundgaard, S.R. Kurtz, D.S. Ginley, D.C. Olson, M.T. Lloyd, P. Morvillo, E.A. Katz, A. Elschner, O. Haillant, T. R. Currier, V. Shrotriya, M. Hermenau, M. Riede, K.R. Kirov, G. Trimmel, T. Rath, O. Inganäs, F. Zhang, M. Andersson, K. Tvingstedt, M. Lira-Cantu, D. Laird, C. McGuiness, S.J. Gowrisanker, M. Pannone, M. Xiao, J. Hauch, R. Steim, D. M. DeLongchamp, R. Rösch, H. Hoppe, N. Espinosa, A. Urbina, G. Yaman-Uzunoglu, J.-B. Bonekamp, A.J.J.M.v. Breemen, C. Girotto, E. Voroshazi, F. C. Krebs, Consensus stability testing protocols for organic photovoltaic materials and devices, Sol. Energy Mater. Sol. Cells 95 (2011) 1253–1267, https://doi.org/10.1016/j.solmat.2011.01.036.
[28] S. Hong, H. Kang, G. Kim, S. Lee, S. Kim, J.-H. Lee, J. Lee, M. Yi, J. Kim, H. Back, J.-R. Kim, K. Lee, A series connection architecture for large-area organic photovoltaic modules with a 7.5% module efficiency, Nat. Commun. 7 (2016) 10279, https://doi.org/10.1038/ncomms10279.
[29] Y.-J. Heo, Y.-S. Jung, K. Hwang, J.-E. Kim, J.-S. Yeo, S. Lee, Y.-J. Jeon, D. Lee, D.-Y. Kim, Small-molecule organic photovoltaic modules fabricated via halogen-free solvent system with roll-to-roll compatible scalable printing method, ACS Appl. Mater. Interfaces 9 (2017) 39519–39525, https://doi.org/10.1021/acsami.7b12420.
[30] Y.-J. Heo, B. Lim, Y.-S. Jung, K. Hwang, J.-E. Kim, D. Lee, D.-H. Lim, J.M. Park, D.-Y. Kim, Printed large-area photovoltaic modules based on small molecules with different alkyl terminal chains, ACS Appl. Energy Mater. 2 (2019) 8885–8893, https://doi.org/10.1021/acsaem.9b01789.
[31] B. Lim, S.-Y. Han, S.-H. Jung, Y.J. Jung, J.M. Park, W. Lee, H.-S. Shim, Y.-C. Nah, Synthesis and electrochromic properties of a carbazole and diketopyrrolopyrrole-based small molecule semiconductor, J. Ind. Eng. Chem. 80 (2019) 93–97, https://doi.org/10.1016/j.jiec.2019.07.035.
[32] D. Vak, K. Hwang, A. Faulks, Y.-S. Jung, N. Clark, D.-Y. Kim, G.J. Wilson, S. E. Watkins, 3D printer based slot-die coater as a lab-to-fab translation tool for solution-processed solar cells, Adv. Energy Mater. 5 (2015) 1401539, https://doi.org/10.1002/aenm.201401539.
[33] W. Liu, S. Liu, N.K. Zawacka, T.R. Andersen, P. Cheng, L. Fu, M. Chen, W. Fu, E. Bundgaard, M. Jørgensen, X. Zhan, F.C. Krebs, H. Chen, Roll-coating fabrication of flexible large area small molecule solar cells with power conversion efficiency exceeding 1%, J. Mater. Chem. 2 (2014) 19809–19814, https://doi.org/10.1039/C4TA04733H.
[34] A.W. Czanderna, F.J. Pern, Encapsulation of PV modules using ethylene vinyl acetate copolymer as a pottant: a critical review, Sol. Energy Mater. Sol. Cells 43 (1996) 101–181, https://doi.org/10.1016/0927-0248(95)00150-6.
[35] S. Jiang, K. Wang, H. Zhang, Y. Ding, Q. Yu, Encapsulation of PV modules using ethylene vinyl acetate copolymer as the encapsulant, Macromol. React. Eng. 9 (2015) 522–529, https://doi.org/10.1002/mren.201400065.
[36] Y. Li, J. Olsen, K. Nunez-Ortega, W.-J. Dong, A structurally modified perylene dye for efficient luminescent solar concentrators, Sol. Energy 136 (2016) 668–674, https://doi.org/10.1016/j.solener.2016.07.051.
[37] L.H. Slooff, E.E. Bende, A.R. Burgers, T. Budel, M. Pravettoni, R.P. Kenny, E. D. Dunlop, A. Büchtemann, A luminescent solar concentrator with 7.1% power conversion efficiency, Phys. Status Solidi RRL 2 (2008) 257–259, https://doi.org/10.1002/pssr.200802186.
[38] J.E. Lewis, E. Lafalce, P. Toglia, X. Jiang, Over 30% transparency large area inverted organic solar array by spray, Sol. Energy Mater. Sol. Cells 95 (2011) 2816–2822, https://doi.org/10.1016/j.solmat.2011.05.037.
[39] H. Jin, C. Tao, M. Velusamy, M. Aljada, Y. Zhang, M. Hambsch, P.L. Burn, P. Meredith, Efficient, large area ITO-and-PEDOT-free organic solar cell sub-modules, Adv. Mater. 24 (2012) 2572–2577, https://doi.org/10.1002/adma.201104896.

[40] Y. Li, Y. Sun, Y. Zhang, Boosting the cost-effectiveness of luminescent solar concentrators through subwavelength sanding treatment, Sol. Energy 198 (2020) 151–159, https://doi.org/10.1016/j.solener.2020.01.038.
[41] Y. Li, Y. Sun, Y. Zhang, Regional measurements to analyze large-area luminescent solar concentrators, Renew. Energy 160 (2020) 127–135, https://doi.org/10.1016/j.renene.2020.06.121.
[42] S. Holliday, C.K. Luscombe, Low boiling point solvent additives for improved photooxidative stability in organic photovoltaics, Adv. Electron. Mater. 4 (2018) 1700416, https://doi.org/10.1002/aelm.201700416.